Impedance Spectroscopy of Perovskite Solar Cells With SnO$_2$ Embedding Graphene Nanoplatelets

Ilaria Matacena [ORCID], Laura Lancellotti [ORCID], Santolo Daliento [ORCID], Brigida Alfano [ORCID], Antonella De Maria [ORCID], Vera La Ferrara [ORCID], Lucia V. Mercaldo [ORCID], Maria Lucia Miglietta [ORCID], Tiziana Polichetti [ORCID], Gabriella Rametta [ORCID], Gennaro V. Sannino [ORCID], Paola Delli Veneri [ORCID], and Pierluigi Guerriero [ORCID]

Abstract—**Characterizing the electron transport layer (ETL)/perovskite interface in perovskite solar cells (PSCs) is of paramount importance for their overall performance. In this article the effect of different concentrations of graphene nanoplatelets in addition to SnO$_2$ is investigated by considering degradation over time. PSCs behavior is monitored by collecting dark current–voltage curves as fabricated and after two months. A deeper insight is gained through impedance spectroscopy analysis. From Nyquist plots equivalent circuit models and the corresponding time constants are extracted. Moreover, resistive part of the impedance associated with high frequency has been related to static shunt resistance, assessing one of the considered ETL doping concentration as the more suitable choice to reduce degradation.**

Index Terms—**Impedance spectroscopy (IS), perovskite solar cells (PSCs).**

I. INTRODUCTION

PEROVSKITE solar cells (PSCs) have experienced a continuous grown in interest in the last years, thanks to the huge increase in the efficiency of this new type of solar cells. Indeed, a stable efficiency of 25.7% [1] has been reported in few years, attesting this new emerging class of solar cells as a protagonist of the next generation of photovoltaics. The large interest in such solar cells lies in the intrinsic properties of the perovskites. These materials enable ambipolar carrier transport [2], possessing high electron/hole mobility [3] and large diffusion length [4]. Perovskites materials also benefit from a tunable

Ilaria Matacena, Santolo Daliento, and Pierluigi Guerriero are with the Department Electrical Engineering and Information Technology, University of Naples "Federico II", 80125 Naples, Italy (e-mail: ilaria.matacena@unina.it; daliento@unina.it; pierluigi.guerriero@unina.it).

Laura Lancellotti, Brigida Alfano, Antonella De Maria, Vera La Ferrara, Lucia V. Mercaldo, Maria Lucia Miglietta, Tiziana Polichetti, Gabriella Rametta, Gennaro V. Sannino, and Paola Delli Veneri are with the ENEA, Research Center Portici, 80055 Portici, Italy (e-mail: laura.lancellotti@enea.it; brigida.alfano@enea.it; antonella.demaria@enea.it; vera.laferrara@enea.it; lucia.mercaldo@enea.it; mara.miglietta@enea.it; tiziana.polichetti@enea.it; gabriella.rametta@enea.it; gennarovsannino@gmail.com; paola.delliveneri@enea.it).

bandgap [5] and a high absorption coefficient [7]. Moreover, this technology has the great advantage of combining high efficiency with low-cost materials and processes [6], [8].

Despite the rapid progress of this technology, there are some challenges to overcome, such as current–voltage hysteresis and long-term stability [9]. The latter issue seems to be influenced by degradation of the perovskite [10] attributable to phenomena occurring in the perovskite material due to external stimulus [11], [12], [13] or intrinsic chemical composition [14], [15]. As a matter of fact, material stability is greatly affected by the quality of the interface embedded in PSC. In such solar cells, a crucial role is represented by the interface forming between the perovskite layer, which absorbs the incident spectrum and the transport layers, which are responsible of the electron and hole transport, respectively, electron transport layer (ETL) and hole transport layer (HTL). The interface between perovskite/ETL is one of the most critical in this technology [16]. ETL are usually made of SnO$_2$ [17], deposited through low-temperature procedures [18]. Such processes may generate traps in the SnO$_2$ [19], lowering the quality of the interface [20]. A proposed solution to lower trap concentration involves the doping of the ETL layer. More in detail, it has been found that the use of graphene [21] as material for SnO$_2$ dopant has a beneficial effect on the overall performance [22], [23], [24], [25]. The ETL modification by graphene (G-SnO$_2$) results in the enhancement of carrier collection and improvement solar cell stability. This can be attributed to the incorporation of graphene in the ETL, which results both in the enhancement of the electron mobility, meaning a higher carriers extraction capability, and in the suppression if the interfacial charge recombination, due to its passivation effect [26], [27]. In previous work, [28], we compared a PSC, without G-SnO$_2$, with the PSCs embedding G-SnO$_2$, showing that the incorporation of graphene nanoplatelets resulted in an improvement of the PSC performance. To investigate PSCs degradation several techniques can be employed. Among these, impedance spectroscopy (IS) has been extensively exploited as a powerful and nondestructive electrical technique to characterize a wide variety of devices, ranging from batteries [26], [27], [28], [29], [30], [31], [32], [33] and power devices [34], [35], [36] to solar cells [37], [38], [39], [40], [41], [42], [43], [44]. This technique has been applied to PSCs during last years with various aims [46], [47], [48], [49], [50], [51], [52]. IS consists in the investigation in frequency of the ac behavior of a device under test. It is performed by imposing a stationary condition on
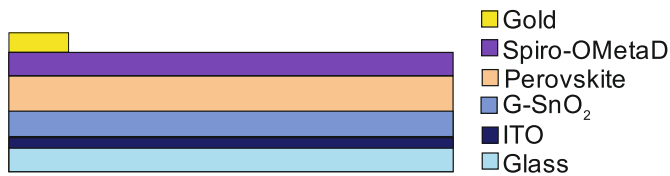
Fig. 1.   Structure of the PSCs considered in this work. The structure is not to scale.

the device through a fix dc bias and, at the same time, an ac small signal is superimposed at different frequencies. The strength of this characterization method consists in the possibility to decouple various phenomena taking place in the device by performing a single measurement. Moreover, IS allows to extract information on a specific interface from the external overall measured impedance [45]. By monitoring the impedance spectra in a time period, it is possible to investigate the mechanisms causing the degradation over time of the device under test [28]. In addition, impedance measurement can be easily achieved by means of not critical setup.

In this work, the effect of two different concentrations of graphene nanoplatelets in addition to SnO₂ on PSC degradation is investigated. Performance of PSC embedding the two different concentrations of G-SnO₂ are evaluated as fabricated and after two months. It is first considered the sample embedding the lower dopant concentration. Experimental current-voltage (I–V) dark characteristics show a change in the solar cell behavior. IS allowed to unravel the mechanisms behind this degradation. High frequency (HF) impedance spectra are related to recombination phenomena and its resistive part can be associated with shunt resistance. Due to the degradation issues, the dopant concentration has been increased and the same analysis is performed on the obtained solar cell. Results demonstrated a decreased degradation, which corresponds to a reduced recombination. The static series resistance is calculated from IS analysis, attesting such treatment to be also beneficial to such parameter.

The rest of this article is organized as follows. In Section II, technological details are explained, and experimental setups are described. Dark current–voltage curves and IS data are presented and discussed in Section III. In the same section the recombination time constants, as well as series resistance, are calculated for both samples. Finally, Section IV concludes this article.

II. PSCs Fabrication and Experimental Setup

The structure of the perovskite solar cell subject of this work is shown in Fig. 1. As it can be seen, the considered structure consists of a single junction perovskite cell with n-i-p architecture were built on glass substrates coated with ITO (Kintec, 10 Ω/sq), in accordance with the procedure described in previous work [53]. Before deposition of the ETL, a UV-ozone treatment was carried out to increase the wettability of the substrate. In the PSCs considered in this work, graphene nanoplatelets were added to ETL. Graphene was obtained by exfoliation of graphite flakes in a hydro-alcoholic mixture [54]. More specifically, natural graphite flakes were dispersed in H₂O/IPA, 7:1 v/v, with

an initial concentration of 1 mg/ml. The dispersion was treated in an ultrasonic bath for 48 h. The nonexfoliated solid residue was removed by centrifugation at 1000 r/min for 45 min and 50% of the supernatant suspension was collected. This suspension was lyophilized to obtain graphene nanoflakes as solid phase. Two suspensions of graphene nanoflakes in H₂O/IPA were prepared, #1 and #2, with a concentration of 0.05 and 0.5 mg/mL, respectively. Then, 1 mL of commercial SnO₂ dispersion was added to 4.5 mL of deionized water and 0.5 mL of suspension #1 or #2. These suspensions were used to realized two series of samples with two different ETLs by spin coating (6000 r/min–6000 r/min/s-50 s). The substrates were annealed at 100 °C for about 5 min and at 150 °C for 1 h. Batches were prepared on the same day to maintain similar environmental conditions.

The perovskite film was deposited by spin coating in a glove box with nitrogen following the one-step antisolvent procedure. The perovskite precursor solution was prepared by mixing PbI₂ (1.10 M), PbBr₂ (0.22 M), formamide iodide (1.05 M), methyl ammonium bromide (0.20 M) in dimethylformamide (N, N-dimethylformamide): dimethylsulfoxide (4:1, v/v), and adding a 1.50 M solution of CsI in DMSO to obtain molar ratio of 5%. Chlorobenzene (CBZ) was chosen as antisolvent, added to the substrate a few seconds before the end of the spin coating. The samples were annealed at 100 °C for 1 h. The Spiro-OMeTAD was then applied to the perovskite layer by spin coating in a nitrogen glove box. The Spiro-OMeTAD solution in CBZ was previously doped with 4-t-butylpyridine, a Li-TFSI solution and an FK 209 Co (III) TFSI solution. The solar cells were finally closed by evaporating gold (80 nm). In the following, PSC obtained using suspension #1 will be addressed as sample #1, while the structure obtained with suspension #2 will be called as sample #2. Samples were initially stored in a dark box with about 30% RH and were subsequently stored in law vacuum, in according to the procedure reported previously [53]. The described devices have been characterized through dark current–voltage characteristics and IS analysis. The experimental setup used to measure the dark I–V curves is composed by a Keithley 236 Source Measure Unit. PSCs under test have been placed in a darkened box electrically connected to the multimeter. Voltage has been swept from –0.5 to 1.2 V with a step of 5 mV. Each point has been acquired after a time of 300 ms. Illuminated current–voltage characteristics were obtained at AM1.5G by exposing the solar cells in ambient air under a class AAA dual-lamp WACOM WXS-155S-L2 solar simulator equipped with a 1000 W Xenon lamp and a 400 W Halogen lamp. The irradiated area was ~0.1 cm². External voltage was applied while recording the generated photocurrent using a Keithley 2651A Source Measure Unit. Impedance spectra have been carried out in dark condition using a Solartron 1260 Impedance Analyzer, Fig. 2(a). To obtain impedance curves, for a certain dc bias, an ac small signal is imposed with a frequency varying from 1 to 100 mHz with a logarithmic sweep, Fig. 2(b). The superimposed ac signal amplitude is set to 10 mV in order to ensure linearity while avoiding electrical noise, which arises especially at low frequencies. In the following, the curves have been collected for dc bias ranging from −0.2 to 0.2 V in order to explore both reverse and forward bias regions.
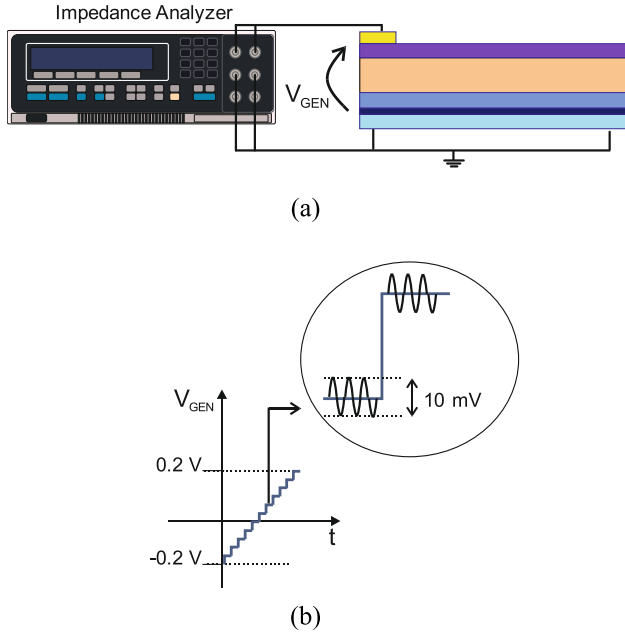
(a)

(b)

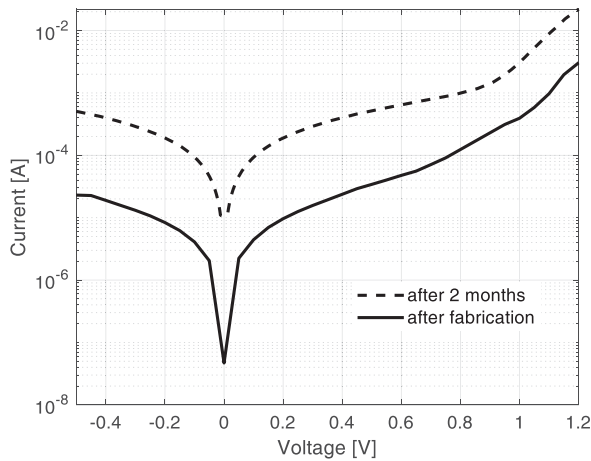Fig. 2. (a) Experimental setup used for impedance measurements and (b) applied voltage signal.

Fig. 3. Dark *I–V* curves obtained from sample #1 after fabrication (line) and two months later (dashed line).
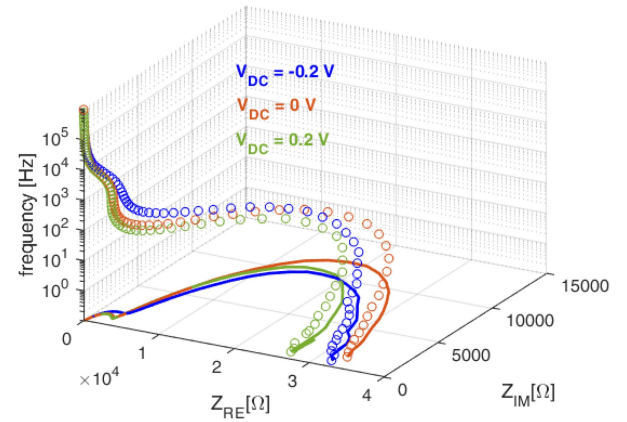

Fig. 4. 3-D representation of experimental Nyquist plots obtained from sample #2 (graphene TQ) just after fabrication.

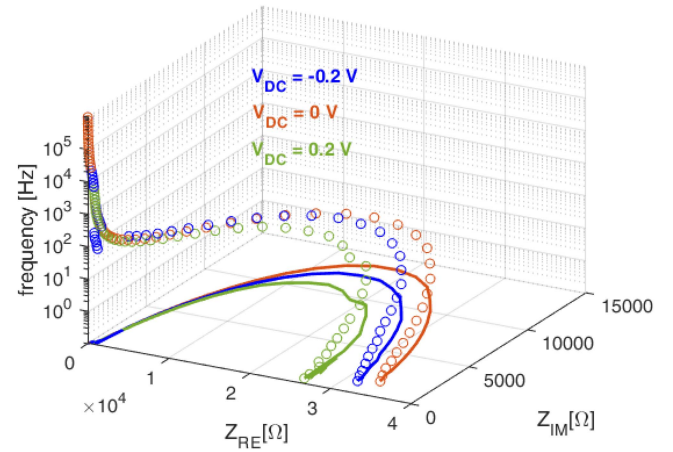Fig. 5. 3-D representation of experimental Nyquist plots obtained from sample #2 (graphene TQ) after 2 months.

III. EXPERIMENTAL RESULTS

At first, it has been considered the PSC obtained with lower graphene nanoplatelets concentration, sample #1. To characterize the fabricated structure, it has been employed the most immediate technique consisting in the evaluation of dark *I–V* curves, Fig. 3. These characteristics have been carried out as fabricated (line in Fig. 3) and the over two months (dashed line in the same figure). The reverse current of the dashed curve is considerably higher with respect to the full line. The two curves obtained from the same sample over the period of two months are different, suggesting that a variation occurred in the cell performance. In order to gain a deeper insight in the origin of such variation, it has been performed an impedance analysis. In the following Nyquist plot are presented in the form of a 3-D plot, making explicit the frequency information. Impedance acquired from sample #1 just after fabrication is presented in Fig. 4. Same graph is reported for the data acquired after two months, Fig. 5.

It is possible to notice that in both graphs, the bigger circumference corresponds to the low frequency (LF), which consists in the range [100 mHz, 1 kHz] for the considered cell, while the smaller circle is associated with the HF range. It is possible to interpret the impedance data in term of equivalent circuit [55], where each impedance arc can be associated with the parallel of a resistance and a capacitance (RC pair), while the shift on the *x*-axis from the origin represents a series resistance. Since the impedance spectra is composed of two semicircles in both Figs. 4 and 5, the equivalent circuit configuration consists of two RC pairs with a series resistance, Fig. 6. Although the same circuit configuration can be employed to describe the ac behavior of the structure over time, the lumped elements change in the two cases. Actually, by comparing sample #1 data measured over time on the same graph, Fig. 7, it can be appreciated how the impedance drastically modifies within two months. More in detail, the maximum of the real part of the impedance, Z_{REmax},
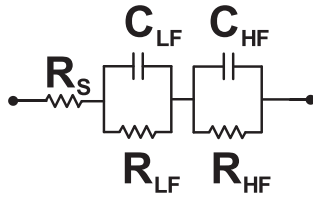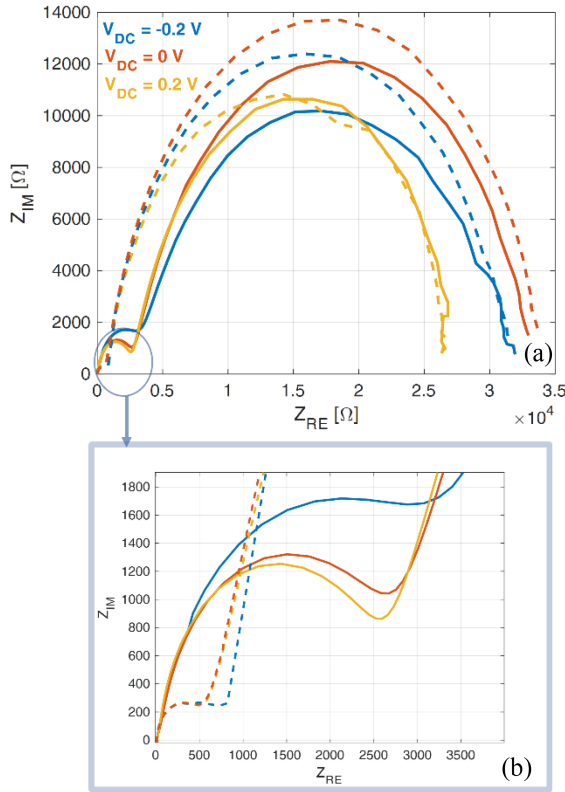
Fig. 6.   Equivalent circuit model.

Fig. 7.   (a) Experimental Nyquist plots obtained from sample #1 just after fabrication (full lines) and after 2 months (dashed lines). (b) Highlight of the HF impedance spectra.

is much smaller after two months with respect to the pristine curve.

As widely accepted, the static behavior of a solar cell can be accurately described using the equivalent circuit referred as five-parameter model. In this model, the recombination mechanisms are taken into account through a lumped parallel resistance, known as shunt resistance R_{sh}. This suggests that, in the static operation, recombination mechanisms considered through the shunt resistance should not vary with the dc value. On the other hand, the recombination phenomena are dominated by the time constants. Hence, in the dynamic operation, as the frequency of the ac signal becomes comparable with the recombination/generation rates, capacitive effects appear in the measured impedance. Consequently, the dynamic behavior of the recombination mechanisms can be modeled as a RC pair where the resistance is independent from the voltage bias and the capacitance is dominating the HF behavior. This assertion
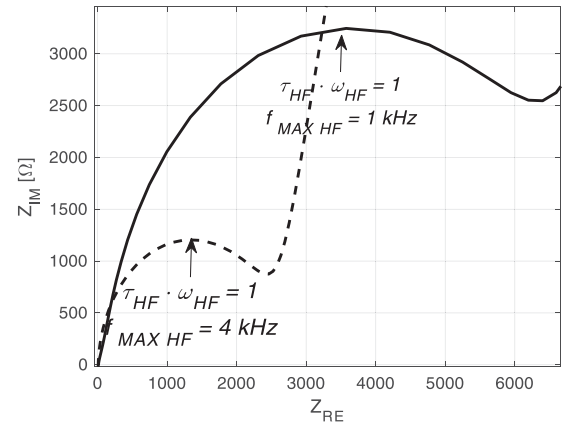
Fig. 8.   Zoom of the Nyquist plot of Fig. 7 obtained just after fabrication (full line) and after two months (dashed line) for a VDC = 0 V.

TABLE I
TIME CONSTANTS OBTAINED FROM SAMPLE #1

Sample #1	τ_{HF} [s]
After fabrication	$1.60 \cdot 10^{-4}$
After 2 months	$4.00 \cdot 10^{-5}$

is corroborated by the experimental data of Fig. 7, where in the HF range is always present a semicircle, which is substantially independent from dc voltage. Therefore, in the model of Fig. 6, the HF RC pair is to be considered related to the recombination mechanisms and R_{HF} can be associated with the shunt resistance of the solar cell.

The diameter of the HF arc, i.e., R_{HF}, reduces after two months of about the 80%. This means that R_{sh} decreases over time and recombination mechanisms becomes more relevant.

Each RC pair has an associated time constant, τ, related to physical phenomena taking place in the solar cell under test. The time constant associated with HF arc, τ_{HF}, is related to the recombination mechanisms and it can be calculated as follows:

$$\tau_{\text{HF}} = R_{\text{HF}} \cdot C_{\text{HF}}. \tag{1}$$

When the imaginary part of the impedance, Z_{IM}, reaches its maximum in the HF arc, the following equation can be written:

$$\tau_{\text{HF}} \cdot \omega_{\text{HF}} = 1 \tag{2}$$

where $\omega = 2\pi f_{\text{MAX HF}}$. The HF arcs are magnified for the data aquired after fabrication and over two months in Fig. 8 and $f_{\text{MAX HF}}$ is shown for both curves, while the extracted τ_{HF} values are reported in Table I. It can be seen that the τ_{HF} reduces of one order of magnitude over time, suggesting that recombination process becomes faster in the structure.

Due to the observed degradation issue, a higher concentration of graphene nanoplatelets has been taken into account and sample #2 has been studied. The dark I–V curves are carried out as fabricated and after two months and results are presented in Fig. 9. The two curves behaves similarly and there is no remarkable discrepancy between them. Thus, this seems to suggest that
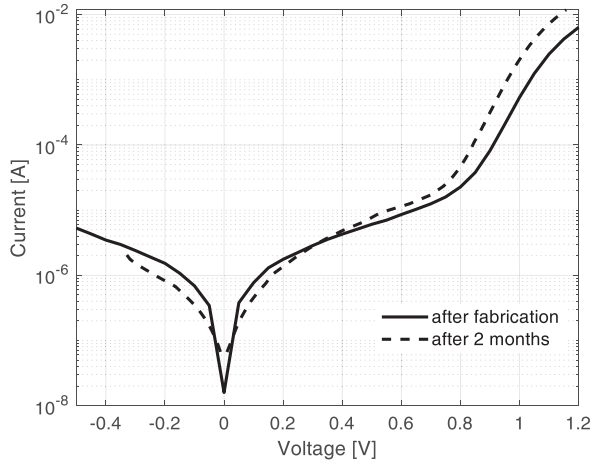
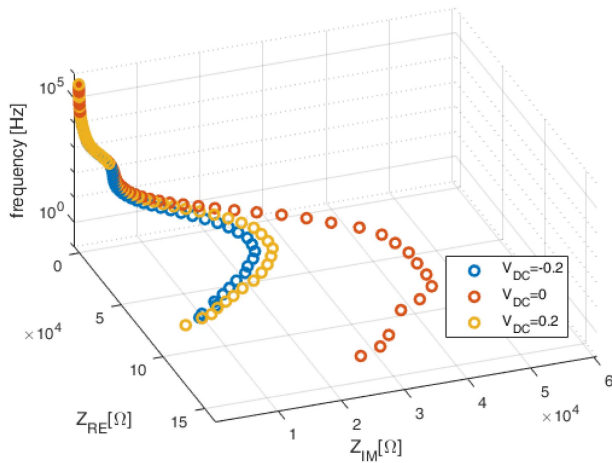Fig. 9. Dark *I–V* curves obtained from sample #2 after fabrication (line) and two months later (dashed line).

Fig. 10. 3-D representation of experimental Nyquist plots obtained from sample #2 just after fabrication.
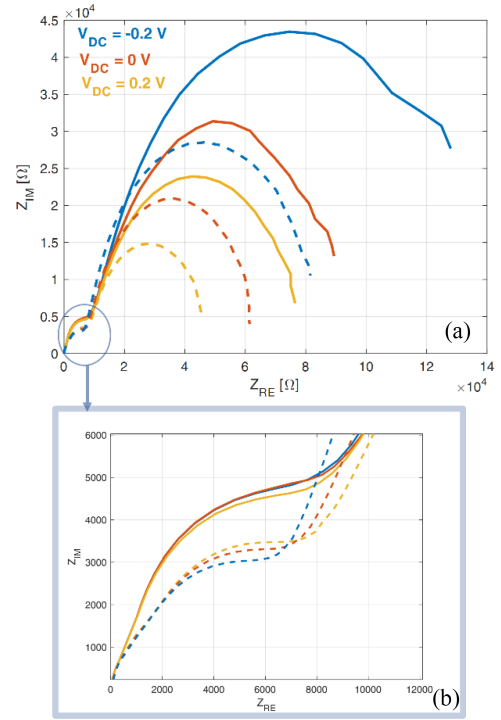

Fig. 11. (a) Experimental Nyquist plots obtained from sample #2 just after fabrication (full lines) and after 2 months (dashed lines). (b) Highlight of the HF impedance spectra.
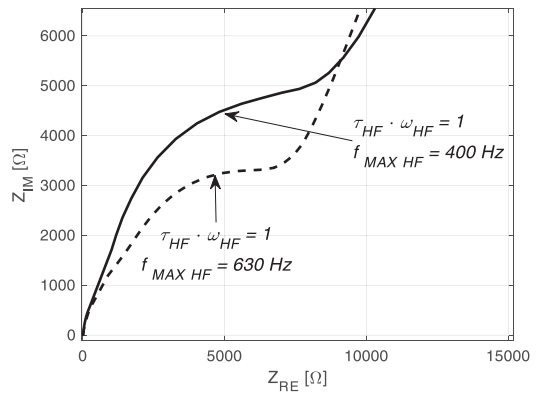

Fig. 12. Zoom of the Nyquist plot of Fig. 12 obtained just after fabrication (full line) and after two months (dashed line) for a VDC = 0 V.

sample #2 behavior over time does not substantially modify. In order to confirm this trend, the same impedance analysis already performed on sample #1 is carried out also for sample #2.

The impedance spectra obtained after fabrication and after two weeks are shown, respectively, in Figs. 10 and 11. To fairly compare the impedance spectra, Nyquist plots are superimposed in Fig. 11.

The equivalent circuit associated with sample #2 impedance spectra of Fig. 11 is composed by two RC pairs and a series resistance, as it was the case for sample #1, Fig. 6. The HF arc only reduces of the 30% after two months, Fig. 12, which represents a much lower decrease compared with sample #1. The corresponding time constants calculated for sample #2 are reported in Table II. Their values do not exhibit a great variation over time, and they are higher than those obtained for sample #1 in every cases. This outcoming could imply that over time the recombination process is not becoming dominant in the case of sample #2. Moreover, the recombination mechanisms seem to be less significant in this latter case. Thus, comparing the Nyquist plots acquired over time, it is possible to relate the changes occurring in the impedance spectra with the recombination phenomena taking place in the device in the consider time period.

It worth to note that when the frequency tends to very small value, ideally it tends to zero, i.e., to the static condition, then, the real part of the impedance reaches its maximum, which is equal to the sum of all the resistances

$$Z_{REmax} = R_S + \sum_{i=1}^{n} R_i \qquad (3)$$

where $n = 2$ in our case since there are two RC pairs in both the extracted equivalent circuit.

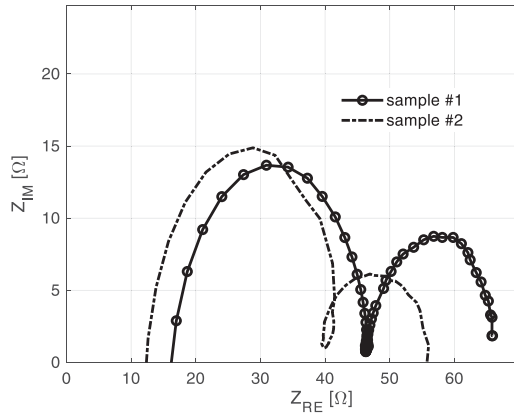| Sample #2	τ_{HF} [s]
After fabrication	$4 \cdot 10^{-4}$
After 2 months	$2.5 \cdot 10^{-4}$

Fig. 13. Nyquist plots obtained from sample #1 (dot line) and sample #2 (markers) with a dc bias equal to 1 V.

	Sample #1	Sample #2
	R_{SERIES} [Ω]	
I–V dark	62.6	50.0
Nyquist plot	66.5	55.0

Considering previous equation, the maximum of the real part of the measured impedance represents the series resistance, R_{SERIES}, extracted in the static condition. In Fig. 13, it is presented the Nyquist plots obtained from both samples imposing a dc bias of 1 V and using same setup of Fig. 2. As it is possible to observe, the Nyquist plot related to sample #1 has a higher Z_{REmax} compared with sample #2. Series resistances of both samples are estimated from IS and I–V dark curves and their values are listed in Table III. As preannounced from visual inspection, sample #1 has a higher series resistance with respect to sample #2.

The photovoltaics performance of the two considered devices measured after fabrication are reported in Fig. 14. In the same Figure, the inset reports the extracted parameters for both PSCs. The open-circuit voltage arising from sample #2 is higher with respect to sample #1. This can be associated with the decrease of recombination due to the incorporation of higher quantity of graphene nanoplatelets in the ETL. Graphene nanoplatelets have been found to provide segregated traps states in SnO$_2$ which acts as localized reservoirs, i.e., avoiding recombination, and they enable an efficient electrons transport. Graphene hydrophobicity
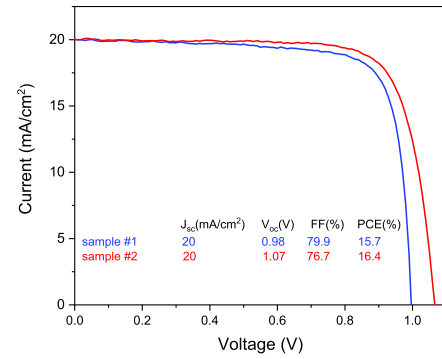

Fig. 14. I–V curves obtained from sample #1 (blue line) and sample #2 (red line). The inset shows the photovoltaic parameters.

is also view as one of the most important aspects, as it postpones the perovskite degradation, improving the device stability [57], [58].

IV. CONCLUSION

In this article, two PSCs embedding ETL doped with two different concentrations of graphene nanoplatelets are studied and compared over time. IS analysis has been used to gain a better insight in the I–V experimental data. From Nyquist plots, the equivalent circuit model to describe ac behavior of the PSC under test has been extracted. The circuit configuration found for both the considered PSCs is composed by a series resistance and two RC pairs, each of them associated with the HF or LF range. Impedance behavior in HF has been related to recombination mechanisms taking place in the solar cell and its resistive part is found to be an indication of the shunt resistance. Results have shown that the sample with higher graphene nanoplatelets concentration registered a lower degradation over time and higher time constants, implying a lower recombination in the device compared with the other sample. Furthermore, it has been shown that series resistance arising in the static condition can be evaluated by Nyquist plots carried out at the dc value of interest. These values have been extracted and compared for both samples. Results shows that an increased graphene nanoplatelets concentration lowers the series resistance, improving the overall performance.

REFERENCES

[1] M. Green et al., "Solar cell efficiency tables (version 57)," *Prog. Photovolt.: Res. Appl.*, vol. 29, no. 1, pp. 3–15, 2021.

[2] Y. Chen et al., "Efficient and balanced charge transport revealed in planar perovskite solar cells," *ACS Appl. Mater. Interfaces*, vol. 7, no. 8, pp. 4471–4475, 2015.

[3] C. Wehrenfennig et al., "High charge carrier mobilities and lifetimes in organolead trihalide perovskites," *Adv. Mater.*, vol. 26, no. 10, pp. 1584–1589, 2010.

[4] Q. Dong et al., "Electron-hole diffusion lengths>175 μm in solution-grown CH3NH3PbI3 single crystals," *Science*, vol. 347, no. 6225, pp. 967–970, 2015.

[5] J. H. Noh et al., "Chemical management for colorful, efficient, and stable inorganic–organic hybrid nanostructured solar cells," *Nano Lett.*, vol. 13, no. 4, pp. 1764–1769, 2013.

[6] H. J. Snaith, "Perovskites: The emergence of a new era for low-cost, high-efficiency solar cells," *J. Phys. Chem. Lett.*, vol. 4, no. 21, pp. 3623–3630, 2013.

[7] G.-H. Kim and D. S. Kim, "Development of perovskite solar cells with>25% conversion efficiency," *Joule*, vol. 5, no. 5, pp. 1033–1035, 2021.

[8] K. D. G. I. Jayawardena et al., "'Inorganics-in-organics': Recent developments and outlook for 4G polymer solar cells," *Nanoscale*, vol. 5, no. 18, pp. 8411–8427, 2013.

[9] M. I. H. Ansari, A. Qurashi, and M. K. Nazeeruddin, "Frontiers, opportunities, and challenges in perovskite solar cells: A critical review," *J. Photochemistry Photobiol. C: Photochemistry Rev.*, vol. 35, pp. 1–24, 2018.

[10] S. Kundu and T. L. Kelly, "In situ studies of the degradation mechanisms of perovskite solar cells," *EcoMat*, vol. 2, no. 2, 2020, Art. no. e12025.

[11] T. A. Berhe et al., "Organometal halide perovskite solar cells: Degradation and stability," *Energy Environ. Sci.*, vol. 9, no. 2, pp. 323–356, 2016.

[12] C. C. Boyd et al., "Understanding degradation mechanisms and improving stability of perovskite photovoltaics," *Chem. Rev.*, vol. 119, no. 5, pp. 3418–3451, 2018.

[13] S. P. Dunfield et al., "From defects to degradation: A mechanistic understanding of degradation in perovskite solar cell devices and modules," *Adv. Energy Mater.*, vol. 10, no. 26, 2020, Art. no. 1904054.

[14] N. Ahn et al., "Trapped charge-driven degradation of perovskite solar cells," *Nature Commun.*, vol. 7, no. 1, 2016, Art. no. 13422.

[15] T. Baiatu, R. Waser, and K.-H. Härdtl, "Dc electrical degradation of perovskite-type titanates: III, a model of the mechanism," *J. Amer. Ceram. Soc.*, vol. 73, no. 6, pp. 1663–1673, 1990.

[16] M. F. M. Noh et al., "The architecture of the electron transport layer for a perovskite solar cell," *J. Mater. Chem. C*, vol. 6, no. 4, pp. 682–712, 2018.

[17] L. Xiong et al., "Review on the application of SnO_2 in perovskite solar cells," *Adv. Funct. Mater.*, vol. 28, no. 35, 2018, Art. no. 1802757.

[18] Y. Bai et al., "Low temperature solution-processed Sb: SnO_2 nanocrystals for efficient planar perovskite solar cells," *ChemSusChem*, vol. 9, no. 18, pp. 2686–2691, 2016.

[19] K. G. Godinho, A. Walsh, and G. W. Watson, "Energetic and electronic structure analysis of intrinsic defects in SnO_2," *J. Phys. Chem. C*, vol. 113, no. 1, pp. 439–448, 2009.

[20] L. Zuo et al., "Tailoring the interfacial chemical interaction for high-efficiency perovskite solar cells," *Nano Lett.*, vol. 17, no. 1, pp. 269–275, 2017.

[21] X. Dai et al., "Focussed review of utilization of graphene-based materials in electron transport layer in halide perovskite solar cells: Materials-based issues," *Energies*, vol. 13, no. 23, 2020, Art. no. 6335.

[22] S. Sidhik et al., "Interfacial engineering of TiO2 by graphene nanoplatelets for high-efficiency hysteresis-free perovskite solar cells," *ACS Sustain. Chem. Eng.*, vol. 6, no. 11, pp. 15391–15401, 2018.

[23] D. Shen et al., "Graphene quantum dots decorated TiO2 mesoporous film as an efficient electron transport layer for high-performance perovskite solar cells," *J. Power Sources*, vol. 402, pp. 320–326, 2018.

[24] M. Dadashbeik, D. Fathi, and M. Eskandari, "Design and simulation of perovskite solar cells based on graphene and TiO2/graphene nanocomposite as electron transport layer," *Sol. Energy*, vol. 207, pp. 917–924, 2020.

[25] M. M. Tavakoli et al., "A graphene/ZnO electron transfer layer together with perovskite passivation enables highly efficient and stable perovskite solar cells," *J. Mater. Chem. A*, vol. 7, no. 2, pp. 679–686, 2019.

[26] M. Dadashbeik, D. Fathi, and M. Eskandari, "Design and simulation of perovskite solar cells based on graphene and TiO2/graphene nanocomposite as electron transport layer," *Sol. Energy*, vol. 207, pp. 917–924, 2020.

[27] D. Shen et al., "Graphene quantum dots decorated TiO2 mesoporous film as an efficient electron transport layer for high-performance perovskite solar cells," *J. Power Sources*, vol. 402, pp. 320–326, 2018.

[28] I. Matacena et al., "Impedance spectroscopy analysis of perovskite solar cell stability," *Energies*, vol. 16, no. 13, 2023, Art. no. 4951.

[29] D. Andre et al., "Characterization of high-power lithium-ion batteries by electrochemical impedance spectroscopy. I. Experimental investigation," *J. Power Sources*, vol. 196, no. 12, pp. 5334–5341, 2011.

[30] I. Landa-Medrano et al., "In situ monitoring of discharge/charge processes in Li–O2 batteries by electrochemical impedance spectroscopy," *J. Power Sources*, vol. 249, pp. 110–117, 2014.

[31] M. Itagaki et al., "In-situ EIS to determine impedance spectra of lithium-ion rechargeable batteries during charge and discharge cycle," *J. Electroanalytical Chem.*, vol. 737, pp. 78–84, 2015.

[32] L. Wang et al., "Electrochemical impedance spectroscopy (EIS) study of LiNi1/3Co1/3Mn1/3O2 for Li-ion batteries," *Int. J. Electrochem. Sci.*, vol. 7, no. 1, pp. 345–353, 2012.

[33] W. Choi et al., "Modeling and applications of electrochemical impedance spectroscopy (EIS) for lithium-ion batteries," *J. Electrochem. Sci. Technol.*, vol. 11, no. 1, pp. 1–13, 2020.

[34] L. Maresca et al., "Influence of the SiC/SiO 2 SiC MOSFET interface traps distribution on C–V measurements evaluated by TCAD simulations," *IEEE J. Emerg. Sel. Topics Power Electron.*, vol. 9, no. 2, pp. 2171–2179, Apr. 2021.

[35] T.-L. Wu et al., "Analysis of the gate capacitance–voltage characteristics in p-GaN/AlGaN/GaN heterostructures," *IEEE Electron Device Lett.*, vol. 38, no. 12, pp. 1696–1699, Dec. 2017.

[36] C. Raynaud et al., "Barrier height determination of SiC Schottky diodes by capacitance and current–voltage measurements," *J. Appl. Phys.*, vol. 91, no. 12, pp. 9841–9847, 2002.

[37] I. Matacena et al., "Impedance spectroscopy for the characterization of the all-carbon graphene-based solar cell," *Energies*, vol. 13, no. 8, 2020, Art. no. 1908.

[38] I. Matacena et al., "Forward bias capacitance investigation as a powerful tool to monitor graphene/silicon interfaces," *Sol. Energy*, vol. 226, pp. 1–8, 2021.

[39] J. Bisquert and F. Fabregat-Santiago, "Impedance spectroscopy: A general introduction and application to dye-sensitized solar cells," in *Dye-Sensitized Solar Cells*. Lausanne, Switzerland: EPFL Press, 2010, pp. 477–574.

[40] F. Fabregat-Santiago et al., "Characterization of nanostructured hybrid and organic solar cells by impedance spectroscopy," *Phys. Chem. Chem. Phys.*, vol. 13, no. 20, pp. 9083–9118, 2011.

[41] I. Mora-Sero et al., "Impedance spectroscopy characterisation of highly efficient silicon solar cells under different light illumination intensities," *Energy Environ. Sci.*, vol. 2, no. 6, pp. 678–686, 2009.

[42] L. Lancellotti et al., "Graphene-on-Silicon solar cells with graphite contacts," in *Proc. Int. Conf. Clean Elect. Power*, 2019, pp. 199–203.

[43] I. Matacena et al., "Impedance spectroscopy characterization of a graphene-based solar cell with improved contacts," in *Proc. ELECTRI-MACS: Sel. Papers-Volume 2*, 2020, pp. 363–373.

[44] A. Sacco, "Electrochemical impedance spectroscopy: Fundamentals and application in dye-sensitized solar cells," *Renewable Sustain. Energy Rev.*, vol. 79, pp. 814–829, 2017.

[45] J. R. Macdonald, "Impedance spectroscopy," *Ann. Biomed. Eng.*, vol. 20, no. 3, pp. 289–305, 1992.

[46] D. Pitarch-Tena et al., "Impedance spectroscopy measurements in perovskite solar cells: Device stability and noise reduction," *ACS Energy Lett.*, vol. 3, no. 4, pp. 1044–1048, 2018.

[47] L. Contreras-Bernal et al., "Impedance analysis of perovskite solar cells: A case study," *J. Mater. Chem. A*, vol. 7, no. 19, pp. 12191–12200, 2019.

[48] I. Zarazua et al., "Operating mechanisms of mesoscopic perovskite solar cells through impedance spectroscopy and J–V modeling," *J. Phys. Chem. Lett.*, vol. 8, no. 24, pp. 6073–6079, 2017.

[49] B. Hailegnaw, N. Serdar Sariciftci, and M. C. Scharber, "Impedance spectroscopy of perovskite solar cells: Studying the dynamics of charge carriers before and after continuous operation," *Physica Status Solidi (a)*, vol. 217, no. 22, 2020, Art. no. 2000291.

[50] A. R. Pascoe et al., "Insights into planar CH3NH3PbI3 perovskite solar cells using impedance spectroscopy," *J. Phys. Chem. C*, vol. 119, no. 9, pp. 4444–4453, 2015.

[51] S. R. Raga and Y. Qi, "The effect of impurities on the impedance spectroscopy response of CH3NH3PbI3 perovskite solar cells," *J. Phys. Chem. C*, vol. 120, no. 50, pp. 28519–28526, 2016.

[52] S. M. Abdulrahim et al., "Long-term stability analysis of 3D and 2D/3D hybrid perovskite solar cells using electrochemical impedance spectroscopy," *Molecules*, vol. 25, no. 24, 2020, Art. no. 5794.

[53] V. La Ferrara et al., "The effect of storage cycle on improvement in the photovoltaic parameters of planar triple cation perovskite solar cells," *Mater. Adv.*, vol. 2, no. 16, pp. 5396–5405, 2021.

[54] F. Fedi et al., "A study on the physicochemical properties of hydroalcoholic solutions to improve the direct exfoliation of natural graphite down to few-layers graphene," *Mater. Res. Exp.*, vol. 2, no. 3, 2015, Art. no. 035601.

[55] I. Matacena, "Equivalent circuit extraction procedure from Nyquist plots for graphene-silicon solar cells," in *Proc. 15th Conf. Ph.D. Res. Microelectronics Electron.*, 2019, pp. 273–276.

[56] L. Lancellotti, E. Bobeico, M. D. Noce, P. Delli Veneri, and I. Matacena, "Work function determination of transparent contact for a: Si/c-Si heterojunction solar cells," in *Proc. IEEE Int. Conf. Environ. Elect. Eng. IEEE Ind. Commercial Power Syst. Europe*, 2018, pp. 1–5.

[57] S. Sidhik et al., "Interfacial engineering of TiO2 by graphene nanoplatelets for high-efficiency hysteresis-free perovskite solar cells," *ACS Sustain. Chem. Eng.*, vol. 6, no. 11, pp. 15391–15401, 2018.

[58] M. M. Tavakoli et al., "A graphene/ZnO electron transfer layer together with perovskite passivation enables highly efficient and stable perovskite solar cells," *J. Mater. Chem. A*, vol. 7, no. 2, pp. 679–686, 2019.